nature communications

Article

https://doi.org/10.1038/s41467-024-52952-9

Robust excitonic light emission in 2D tin halide perovskites by weak excited state polaronic effect

Received: 5 February 2024

Accepted: 26 September 2024

Published online: 02 October 2024

Check for updates

Hongzhi Zhou[1,6], Qingjie Feng[2,6], Cheng Sun[1,3], Yahui Li[4], Weijian Tao[1], Wei Tang[5], Linjun Li[5], Enzheng Shi[4], Guangjun Nan[2] ✉ & Haiming Zhu[1,3] ✉

2D perovskites hold immense promise in optoelectronics due to their strongly bound electron-hole pairs (i.e., excitons). While exciton polaron from interplay between exciton and lattice has been established in 2D lead-based perovskites, the exciton nature and behavior in the emerging 2D tin-based perovskites remains unclear. By combining spin-resolved ultrafast spectroscopy and sophisticated theoretical calculations, we reveal 2D tin-based perovskites as genuine excitonic semiconductors with weak polaronic screening effect and persistent Coulomb interaction, thanks to weak exciton-phonon coupling. We determine an excited state exciton binding energy of ~0.18 eV in $n = 2$ tin iodide perovskites, nearly twice of that in lead counterpart, despite of same large value of ~0.2 eV from steady state measurement. This finding emphasizes the pivotal role of excited state polaronic effect in these materials. The robust excitons in 2D tin-based perovskites exhibit excitation power-insensitive, high-efficiency and color-purity emission, rendering them superior for light-emitting applications.

Ruddlesden–Popper 2D layered metal halide perovskites, denoted as $(LA)_2(A)_{n-1}B_nX_{3n+1}$ where n is inorganic layer thickness, have garnered considerable research interests in past few years[1–10]. Segmenting metal halide inorganic layer by long-chain organic cations (LA^+) not only establishes a robust barrier against water vapor erosion and ion migration, but provides tunable structures, compositions, and properties, in particular, strongly bound electron-hole pairs (excitons) arising from dielectric and quantum confinement. Compared to the conventional Pb counterparts which has been extensively investigated in past years, 2D tin halide perovskites with environmental hazard Pb substituted by biocompatible Sn has emerged very recently and exhibited remarkable optoelectronic properties and technological prospects including stable lasing[5], high-mobility field-effect transistors[11,12] and efficient light-emitting diodes with excellent external quantum efficiency[1].

The exciton nature and dynamics at excited state, rather than ground state, lies at the heart of optoelectronic materials and devices. In 2D lead halide perovskites, a general consensus has been reached that photoexcited excitons are dressed by lattice polarization and distortion, forming exciton polarons with screened electron-hole interaction, due to the interaction between exciton and soft, polarizable lattice[13–19]. The formation of exciton polaron has strong impact on the intriguing properties in 2D lead halide perovskites, including the rich exciton spectral structure, anomalous exciton spin relaxation, exciton dissociation and asymmetric light emission[17–22]. Compared to the Pb counterparts, the excited state exciton nature and dynamics in

[1]Department of Chemistry, State Key Laboratory of Extreme Photonics and Instrumentation, Zhejiang Key Laboratory of Excited State Energy Conversion and Storage, Zhejiang University, Hangzhou, China. [2]Department of Physics, Zhejiang Normal University, Jinhua, Zhejiang, China. [3]ZJU-Hangzhou Global Scientific and Technological Innovation Center, Hangzhou, Zhejiang, China. [4]Research Center for Industries of the Future and School of Engineering, Westlake University, Hangzhou, China. [5]State Key Laboratory of Extreme Photonics and Instrumentation, College of Optical Science and Engineering, Zhejiang University Hangzhou, China. [6]These authors contributed equally: Hongzhi Zhou, Qingjie Feng. ✉e-mail: gjnan@zjnu.edu.cn; hmzhu@zju.edu.cn

https://doi.org/10.1038/s41467-024-52952-9

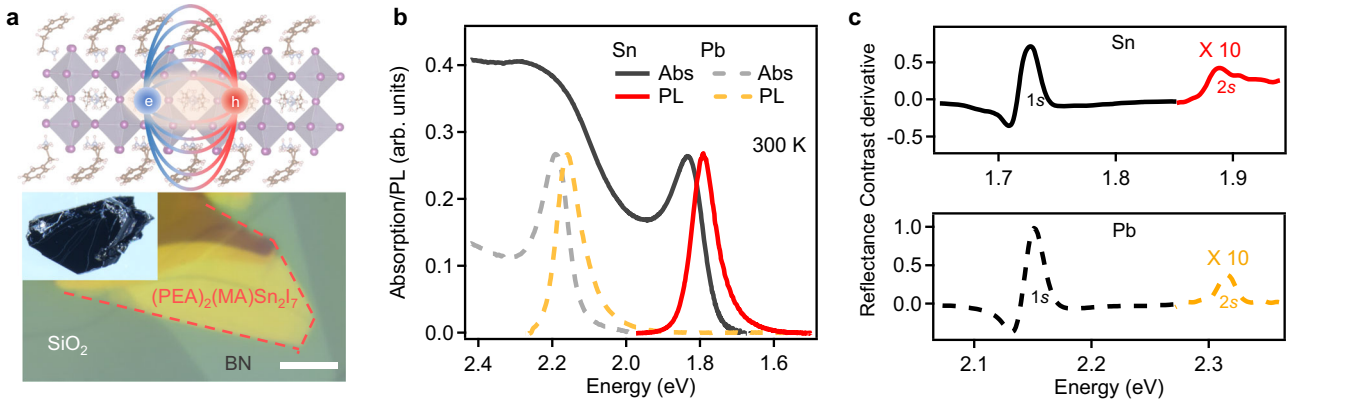

Fig. 1 | Optical characterizations. a Schematic of $(PEA)_2(MA)Sn_2I_7$ and optical image of BN-encapsulated $(PEA)_2(MA)Sn_2I_7$ thin flake (~20 layers). Scale bar: 10 μm. Inset: optical image of $(PEA)_2(MA)Sn_2I_7$ single crystal. **b** The absorption and photoluminescence (PL) spectra of $(PEA)_2(MA)Sn_2I_7$ and $(PEA)_2(MA)Pb_2I_7$ flakes at room temperature. **c** The 1st derivative spectra of the reflectance contrast of $(PEA)_2(MA)Sn_2I_7$ and $(PEA)_2(MA)Pb_2I_7$ at 4 K. The 1s and 2s exciton states are denoted.

the emerging 2D tin halide perovskites have been much less investigated, except for a few recent photophysical comparison studies of 2D ($n = 1$) lead and tin halide perovskite polycrystalline films[23,24]. Recent studies on 2D ($n = 1$) and 3D tin halide perovskites by steady-state spectroscopy measurements suggest a lower exciton binding energy in tin halide perovskites than that in their Pb counterparts[7,24–28], which potentially would favor exciton dissociation into free carriers and thus light-to-electricity conversion, rather than the reverse light emission process. However, this seems to contradict a very recent report of highly efficient light-emitting diodes based on 2D tin halide perovskites[1]. The ultimate question lies in the exact nature and fate of exciton at excited state, especially how it is regulated by exciton-lattice coupling in this family of materials, which remains a puzzle and hinders the design of 2D tin halide perovskites and devices.

Here, we perform a comparison photophysical study between $n = 2$ $(PEA)_2(MA)Sn_2I_7$ (PEA and MA stand for $C_6H_5CH_2CH_2NH_3^+$ and $CH_3NH_3^+$, respectively) and its Pb counterpart $(PEA)_2(MA)Pb_2I_7$ by combining state-of-the-art time-resolved spectroscopy and theoretical simulation to reveal the excited state exciton properties in high quality 2D tin halide perovskite single crystals. Although $(PEA)_2MASn_2I_7$ and the Pb counterpart exhibit a same large exciton binding energy E_b^0 ~ 0.2 eV from steady-state exciton Rydberg series measurement, spin-resolved transient absorption (TA) measurements indicate $(PEA)_2(MA)Sn_2I_7$ retain the strong bound excitons at excited state with an excited state exciton binding energy E_b^* ~ 0.18 eV, in striking contrast to the strongly screened excitons with E_b^* ~ 0.10 eV in Pb counterpart. An in-depth spectroscopy analysis reveals significantly weaker long- and short-range exciton-phonon interactions in $(PEA)_2(MA)Sn_2I_7$, resulting in alleviated excited state polaronic screening effect and robust exciton in 2D tin halide perovskites, which is further confirmed with atomic level excited state stimulations. The robust excited state excitons in 2D tin halide perovskites manifest excitation-power-independent, high-efficiency and high color-purity emission, lending them to light emission and lasing applications.

Results

Sample preparation and characterizations

The high-quality $(PEA)_2(MA)Sn_2I_7$ single crystals (Fig. 1a) were synthesized under N_2 environment by our recently developed method[5]. We mechanically exfoliated optically thin $(PEA)_2(MA)Sn_2I_7$ flakes which were further sandwiched by thin-layer h-BN (Fig. 1a) through van der Waals stacking to protect the 2D perovskite samples from degradation and obtain reliable results[29]. As a reference, we also prepared $(PEA)_2(MA)Pb_2I_7$ sample with only different B site cation using similar method for comparison. The thickness of exfoliated 2D perovskite flakes were characterized by atomical force microscopy which indicates 20–30 layers and thus bulk-like 2D perovskite samples (Supplementary Fig. 1). As shown in Fig. 1b, the absorption spectra of $(PEA)_2(MA)Sn_2I_7$ and $(PEA)_2(MA)Pb_2I_7$ exhibit a strong and sharp peak at 1.831 eV and 2.195 eV, respectively, corresponding to their lowest energy exciton resonance. The photoluminescence (PL) spectra show a corresponding sharp peak with a slight Stokes shift (~0.04 eV). The temperature-dependent PL spectra (Supplementary Fig. 2) and optical characterizations at 80 K (Supplementary Fig. 3) indicate negligible emission from other n or extrinsic edge states even at cryogenic temperature and the absence of phase transition in 80–300 K[6,30,31], confirming high phase purity and high crystal quality.

We first determined the exciton binding energy E_b^0 by conventional steady-state exciton Rydberg series measurement, following previous success on 2D transition metal dichalcogenides and 2D lead halide perovskites[32,33]. We measured the reflectance contrast spectra δR of $(PEA)_2(MA)Sn_2I_7$ and its Pb counterpart at 4 K and the reflectance contrast derivative ($d(\delta R)/dE$) spectra exhibit clearly resolvable 1s and 2s excitonic peaks with similar energy spacing (Δ_{12} ~ 0.16 eV) (Fig. 1c). Thus, the exciton binding energy E_b^0 can be estimated from Δ_{12} by $E_b^0 \approx 1.35\Delta_{12}$[33]. We determined a near identical E_b^0 for $(PEA)_2(MA)Pb_2I_7$ and $(PEA)_2(MA)Sn_2I_7$, 0.22 ± 0.02 eV and 0.21 ± 0.02 eV, respectively. The obtained E_b^0 for $(PEA)_2(MA)Pb_2I_7$ falls into the range of the exciton binding energy in similar materials reported previously (see Supplementary Table 1). We also note the exact value of E_b^0 in 2D perovskites are currently still largely dispersed and requires further experimental and theoretical study, which is beyond the scope of this study focusing on the excited state properties. In the absence of phase transition, E_b^0 can be regarded as a constant from 4 K to room temperature and is about ten times of thermal energy k_BT (k_B is Boltzmann constant and T is temperature) at room temperature[7,8]. According to Saha-Langmuir equation[34,35], at room temperature, more than 95% photoexcitation remain as excitons in both $(PEA)_2(MA)Pb_2I_7$ and $(PEA)_2(MA)Sn_2I_7$ at excitation density of ~10^{11} cm^{-2} (see details in Supplementary Note 1).

The result from steady-state optical measurements does not necessarily reflect the excited state properties because of possible electronic and structural relaxation at excited state. We first resort to PL measurements to get a sense of the excited state behavior in these two 2D metal halide perovskites. The PL quantum yields (QYs) of $(PEA)_2(MA)Sn_2I_7$ and $(PEA)_2(MA)Pb_2I_7$ were measured as a function of excitation power (see details in Supplementary Note 2) and shown in Fig. 2a. Interestingly, PLQY of $(PEA)_2(MA)Sn_2I_7$ remains a near constant of ~60% over three orders of magnitude of excitation power, while that of the Pb counterpart increases continuously from ~1% to ~20% at same

https://doi.org/10.1038/s41467-024-52952-9

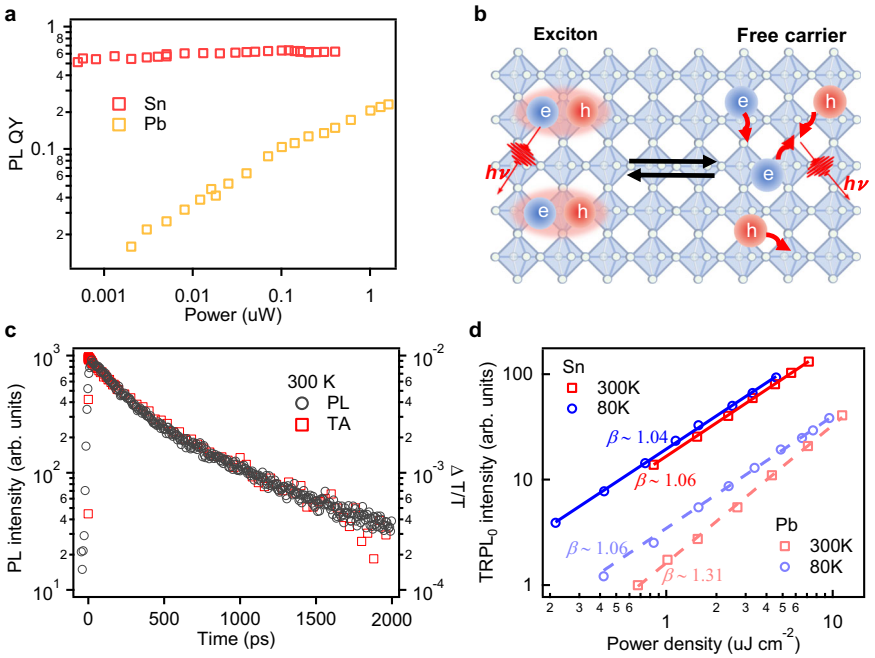

Fig. 2 | Photoluminescence (PL) properties of 2D $(PEA)_2(MA)Sn_2I_7$ and $(PEA)_2(MA)Pb_2I_7$. **a** Photoluminescence quantum yield (PLQY) as a function of excitation power. **b** Schematic of recombination for excitons and free carriers with monomolecular- and bimolecular-like behavior, respectively. **c** PL (black circles) and transient absorption (TA, red squares) kinetics of $(PEA)_2(MA)Sn_2I_7$ thin flake. **d** $TRPL_0$ as a function of laser power density for $(PEA)_2(MA)Sn_2I_7$ and $(PEA)_2(MA)Pb_2I_7$ at 300 K and 80 K, which are extracted from TRPL results in Supplementary Fig. 4. The corresponding power law fitting are shown with a power factor β value listed. The values of $TRPL_0$ have been vertically shifted for clarity.

range. This result suggests pure exciton recombination with monomolecular-like recombination behavior in $(PEA)_2(MA)Sn_2I_7$ where PLQY does not depends on photoexcitation density but the presence of free carrier recombination in the Pb counterpart with bimolecular-like recombination behavior where higher photoexcitation power increases encounter probability of electron and hole carriers thus PLQY (Fig. 2b and Supplementary Note 3)[32,36]. The excited state recombination dynamics can be directly obtained from time-resolved (TR) measurements. Importantly, TR-PL and TA exhibit near-identical kinetics for $(PEA)_2(MA)Sn_2I_7$ but large deviation for $(PEA)_2(MA)Pb_2I_7$ (Fig. 2c and Supplementary Fig. 5), which again suggests dominant excitonic recombination process in $(PEA)_2(MA)Sn_2I_7$ but substantial fraction of dissociated electron and hole recombination process in $(PEA)_2(MA)Pb_2I_7$[19].

Key information about the excited state species is from examining the initial TR-PL intensity at $t = 0$ (denoted as $TRPL_0$), which is proportional to the radiative recombination rate of the initial (~6 ps) photogenerated excited state species since TA kinetics shows no decay in the first 20 ps. Depending on the nature of emitting species, the radiative recombination rate or $TRPL_0$ is proportional to photoexcitation densities ($\propto n_0$) for exciton recombination with monomolecular-like behavior or $\propto n_0^2$ for dissociated electron and hole recombination with bimolecular-like behavior (Fig. 2b)[36]. $TRPL_0$ at 80 and 300 K for both materials are plotted as a function of n_0 in Fig. 2d. A power law fitting ($TRPL_0 \propto n_0^{\beta}$) of experimental results shows $(PEA)_2(MA)Sn_2I_7$ increases linearly with a power factor β of 1.06 and 1.04 at 300 and 80 K, respectively, indicating a robust exciton emission with negligible dissociation at 300 K. In contrast, the Pb counterpart exhibits a similar linear behavior at 80 K ($\beta = 1.06$) but a super-linear relationship ($\beta = 1.31$) at 300 K, confirming high concentration of free electron/hole carriers by exciton thermal dissociation at room-temperature. Similar β values were obtained under near-resonant excitation conditions (Supplementary Fig. 6), demonstrating that the independence of β on excess energy under our experimental conditions.

Exciton spin relaxation

Robust excitonic recombination in $(PEA)_2(MA)Sn_2I_7$ and substantial free carrier recombination in its Pb counterpart indicates their different electron-hole Coulomb interaction strength at excited state, which strongly contradict with their similar E_b^0 of ~0.2 eV extracted from steady state measurements, but suggest different polaronic screening effect at excited state considering their polar and dynamic lattice nature[16–18,35]. As demonstrated by our previous study on 2D $CsPbBr_3$, the excited state polaronic effect and the resulting screened exciton binding energy at excited state (denoted as E_b^*) can be inferred from exciton spin relaxation dynamics[35]. In excitonic systems, the exciton spin relaxation is governed by excited state electron-hole exchange interaction (J) through Maialle-Silva-Sham (MSS) mechanism[35,37–40]. Since J is proportional to E_b^*, exciton spin relaxation rate k_s provides a facial way to quantify E_b^* by

$$k_s \approx \left\langle \Omega_K^2 \right\rangle \tau_p \propto J^2 T \tau_p \propto (E_b^*)^2 T/\Gamma \quad (1)$$

where Ω_K is momentum-dependent Larmor frequency under an effective magnetic field, T denotes temperature and τ_p is momentum scattering time which is inversely proportional to PL linewidth Γ (see details in Supplementary Note 4)[38,39]. The MSS model has described the T-dependent exciton spin relaxation in 2D transition metal dichalcogenides and quantum wells in a quantitative manner[38–41].

We performed spin-resolved femtosecond TA spectroscopy measurements on the exciton spin relaxation dynamics in $(PEA)_2(MA)Sn_2I_7$ at 80–300 K. As shown in Fig. 3a, spin-polarized excitons |+1> (|−1>) can be selectively excited by right (left) circularly polarized pump pulse σ^+ (σ^-) and probed by another circular polarized probe pulse with either same (SCP) or opposite (OCP) circular polarization conditions (see Methods for details)[35,42–46]. Spin-resolved TA results of $(PEA)_2(MA)Sn_2I_7$ at 1.93 eV near-resonant excitation under SCP and OCP conditions are shown in Fig. 3b, with a few representative spectra at indicated delay times (0.4, 4, and 20 ps) in Fig. 3c for better view.

https://doi.org/10.1038/s41467-024-52952-9

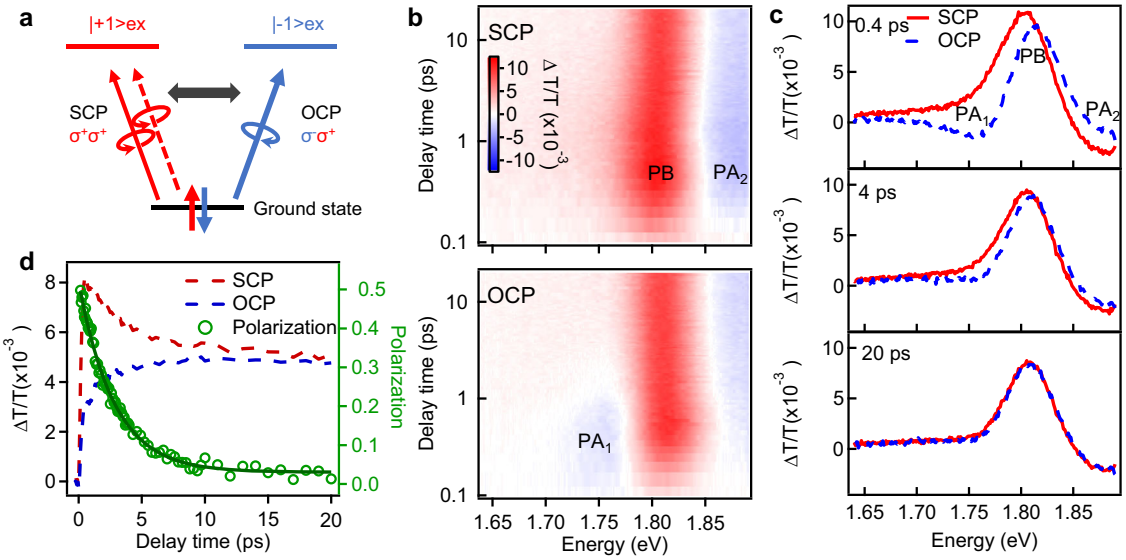

Fig. 3 | Spin-resolved transient absorption spectroscopy of $(PEA)_2(MA)Sn_2I_7$ thin flake at room temperature. a Scheme of spin-resolved TA measurements where spin-polarized excitons are photoexcited by circularly polarized pump pulse and probed by same (SCP) or opposite (OCP) circular polarization. **b** 2D color plot of TA spectra under SCP and OCP conditions at 8 μJ cm^{-2} pump fluence. **c** Spectral evolution for SCP and OCP conditions at representative time delay (0.4, 4, and 20 ps). **d** TA kinetics of SCP and OCP and spin polarization kinetics with single exponential fitting (green line).

The pump fluence was kept low of 3–8 μJ cm^{-2} to ensure TA signal in linear regime.

Generally speaking, TA signal in 2D semiconductors stems from combined band filling effect and Coulombic effect including band renormalization, biexciton effect, and exciton screening[35,42,43]. While band filling and biexciton effect are sensitive to photoexcited exciton occupation in a specific spin state, other effects would apply to both spin states, leading to TA spectral difference. At early time (0.4 ps) after photoexcitation, SCP spectra of $(PEA)_2(MA)Sn_2I_7$ show a dominant photoinduced bleach (PB) feature at exciton resonance due to band filling and band renormalization effect, and a photoinduced absorption (PA_2) at higher energy side due to biexciton repulsion effect (interaction between pump-generated preexisted exciton and probe-induced excitonic transition) from excitons with same spin. On the other hand, OCP spectra show a derivative line shape with PA_1 feature around exciton resonance which can be ascribed to spin-independent band renormalization effect[35,42]. Therefore, the difference on TA spectra between SCP and OCP (i.e. $\delta T_{SCP} - \delta T_{OCP}$) indicates the imbalance of exciton population in +1 and −1 spin states and the creation of spin polarization, which vanishes in ~20 ps (Fig. 3c). To extract the exciton spin relaxation dynamics, we spectrally integrated SCP and OCP spectra at low energy side, where the difference between them is mainly ascribed to the band filling of spin-polarized excitons. The degree of exciton spin polarization (Pol) is calculated by $Pol = (\delta T_{SCP} - \delta T_{OCP})/(\delta T_{SCP} + \delta T_{OCP})$. As shown in Fig. 3d, the spin polarization shows a fast relaxation with a lifetime of 2.79 ± 0.06 ps in $(PEA)_2(MA)Sn_2I_7$. This lifetime is two orders of magnitude shorter than exciton population lifetime, indicating a pure spin relaxation process. This exciton spin relaxation rate is 1–2 orders of magnitude faster than that in 3D bulk Sn-based materials, confirming the dominant electron-hole exchange interaction (MSS) mechanism in 2D perovskites[47]. The spin relaxation rates are also found to depend on pump fluences linearly in $(PEA)_2(MA)Sn_2I_7$ (Supplementary Fig. 7), which further proves the dominant MSS spin relaxation mechanism rather than the Bir–Aronov–Pikus (BAP) or the D'yakonov-Perel (DP) mechanism[35,40,48]. In addition, we performed the same spin relaxation measurement with larger (0.15 eV) or smaller (0.05 eV) excess energies (relative to bandgap) and found that the excess energy mostly affects the initial spin polarization degree and has little effect on the spin relaxation dynamics (Supplementary Fig. 8), which is consistent with previous studies[35,49].

According to Eq. (1), information about excited state electron-hole interaction comes from examining T-dependent exciton spin relaxation kinetics. As shown in Fig. 4a, b, interestingly, by increasing temperature from 80 K to 300 K, exciton spin relaxation is accelerated in $(PEA)_2(MA)Sn_2I_7$ but decelerated in the Pb counterpart. The k_s by single exponential fitting on exciton spin relaxation kinetics are plotted (symbols) in Fig. 4c, d for $(PEA)_2(MA)Sn_2I_7$ and $(PEA)_2(MA)Pb_2I_7$, respectively, showing interestingly opposite T-dependence.

The T-dependent k_s in excitonic system can be described by Eq. (1) and the modeled results assuming a T-independent constant E_b^* are plotted in Fig. 4c, d (line) for $(PEA)_2(MA)Sn_2I_7$ and the Pb counterpart, respectively. The modeled curve has been scaled to match experimental value at 80 K where lattice is mostly frozen and excited state polaronic screening effect can be approximated to be negligible (i.e. $E_b^* = E_b^0$)[50]. Interestingly, the measured k_s for $(PEA)_2(MA)Sn_2I_7$ shows similar trend as the modeled curve but diverges slightly at high temperature while the measured and modeled k_s for $(PEA)_2(MA)Pb_2I_7$ show completely opposite trend. The negative deviation of experimental k_s compared to modeled value assuming constant $E_b^* = E_b^0$ indicates that E_b^* is temperature dependent and significantly screened at elevated temperature. The extent of deviation between experimental and model values allows a quantitative calculation of E_b^* since $k_s \propto (E_b^*)^2$[18,35]. For example, at room temperature, modeled k_s of $(PEA)_2(MA)Pb_2I_7$ is 4.54 times the measured value which yields an excited state exciton binding energy E_b^* of ~ 0.10 ± 0.01 eV. A similar analysis on $(PEA)_2(MA)Sn_2I_7$ provides a E_b^* of ~ 0.18 ± 0.02 eV, almost twice of that in Pb counterpart.

Exciton-phonon interaction

The screened E_b^* well explains different light emission behaviors in $(PEA)_2(MA)Sn_2I_7$ and the Pb counterpart where robust excitonic behavior in the former but partial free carrier behavior in latter have been observed, despite of near identical E_b^0. Because of their polar and dynamic lattice, photoexcited excitons in 2D metal halide perovskites can polarize lattice through exciton-phonon interaction, forming exciton polarons[16,18,19,35]. Depending on the nature and range of exciton-lattice interaction, the excited

https://doi.org/10.1038/s41467-024-52952-9

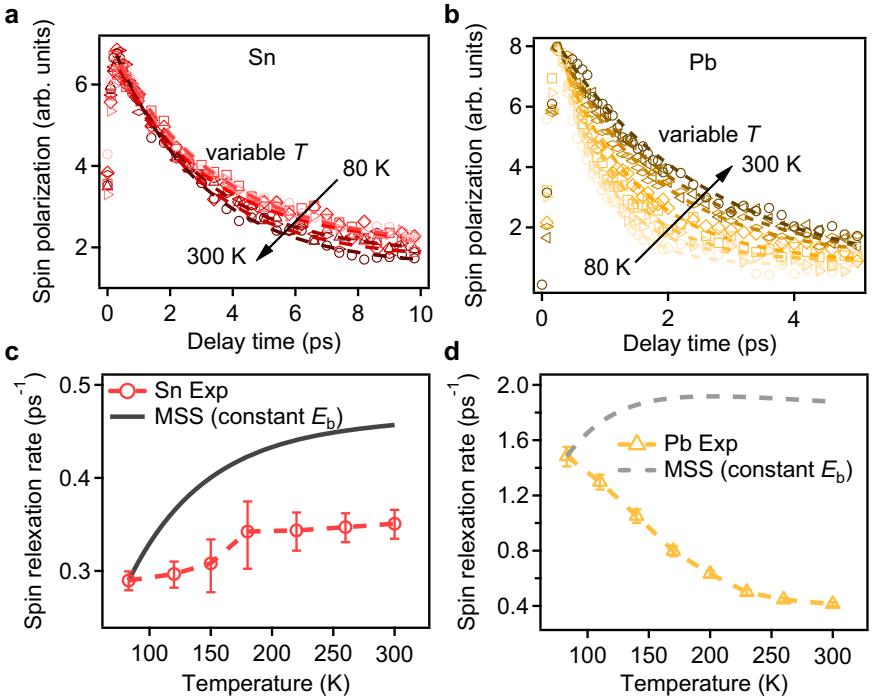

Fig. 4 | Temperature dependence of spin relaxation process. Exciton spin relaxation kinetics at different temperatures from 80 to 300 K and their single exponential fitting of (**a**) $(PEA)_2(MA)Sn_2I_7$ and (**b**) $(PEA)_2(MA)Pb_2I_7$ under near-resonant excitation at 3 μJ cm^{-2} pump fluence. Temperature dependent exciton spin relaxation rate for (**c**) $(PEA)_2(MA)Sn_2I_7$ and (**d**) $(PEA)_2(MA)Pb_2I_7$, showing opposite trend. The error bars represent fitting errors. The lines are modeled temperature dependent exciton spin relaxation rate according to Maialle-Silva-Sham (MSS) mechanism (Eq. (1)) with constant exciton binding energy E_b. The modeled curve has been scaled to match experiment results at 80 K where polaronic effect is negligible.

state polaronic effect can arise from both long-range electrostatic polarization response (Fröhlich interaction) and short-range deformation potential (Holstein interaction)[17,18,20]. The long-range Fröhlich coupling strength is proportional to the lattice polarization response and can be captured by T-dependent PL linewidth[20,51], while the short-range Holstein interaction manifests itself as a Urbach tail on absorption/PL spectra[52–55].

The PL spectra of $(PEA)_2(MA)Sn_2I_7$ and its Pb counterpart at different temperatures (80–300 K) are shown in Fig. 5a, b, respectively, which are broader and more asymmetrical with a prominent low energy tail (Urbach tail) at higher temperature. The full-width-at-half-maximum (FWHM) of PL spectra at different temperatures can be described by a phenomenological equation[31,50,51]

$$\mathrm{FWHM} = \Gamma_0 + \frac{\gamma_{LO}}{[\exp(E_{LO}/k_B T - 1)]} \tag{2}$$

where the first term Γ_0 is T-independent and the second term is contributed by longitudinal optical (LO) phonon scattering with an effective phonon energy E_{LO} and a coupling strength γ_{LO}. By extracting and fitting the FWHM of PL spectra with Eq. (2) (Fig. 5c), we obtain a coupling strength γ_{LO} of 0.072 ± 0.004 eV for $(PEA)_2(MA)Sn_2I_7$, which is smaller than γ_{LO} of 0.095 ± 0.008 eV for its Pb counterpart.

We also analyzed the Urbach tail of PL to quantify the short-range Holstein exciton-phonon coupling strength. The absorption coefficient $\alpha(E,T)$ of Urbach tail below optical band gap can be described by refs. 52–54

$$\alpha(E,T) = \alpha_0 \exp\left(\frac{\sigma(T)(E - E_0)}{k_B T}\right) \tag{3}$$

where α_0 and E_0 are constants, $\sigma(T)$ is a T-dependent steepness parameter which contains exciton-phonon coupling information. With van Roosbroeck-Schockley relation, the Urbach tail of PL can be described by refs. 53,54

$$I_{PL}(E,T) \propto E^2 \exp\left(\frac{\sigma(T) - 1}{k_B T}(E - E_0)\right) \tag{4}$$

Generally, $\sigma(T)$ increases with T and approaches a limit of steepness constant σ_0 at high temperature (e.g., 300 K) by

$$\frac{\sigma(T)}{k_B T} = \frac{2\sigma_0}{\hbar\omega_{ph}} \tanh\left(\frac{\hbar\omega_{ph}}{2k_B T}\right) \tag{5}$$

where $\hbar\omega_{ph}$ is the average energy of interaction phonon modes. Importantly, the steepness constant σ_0 is an inherent property for a certain material and inversely proportional to the Holstein exciton-phonon coupling strength, i.e., smaller σ_0 indicates a stronger short-range exciton-phonon coupling. In high-quality semiconductors with weak electron-phonon coupling strength, σ_0 from PL measurement (corresponding to excited-state configuration, denoted as σ_0^*) and that from absorption measurement (corresponding to ground-state configuration, σ_0^0) have near same value[54,55].

We determined the steepness parameters $\sigma(T)$ for $(PEA)_2(MA)Sn_2I_7$ and its Pb counterpart by fitting PL tails with Eq. (4) (Fig. 5a, b) and the obtained $\sigma(T)$ are plotted in Fig. 5d as a function of temperature. For $(PEA)_2(MA)Sn_2I_7$, $\sigma(T)$ increases with temperature and approaches a limit of 1.58 ± 0.01 (σ_0^*). This value is smaller than that (2.28) in its 3D counterpart[54], which can be ascribed to the increased exciton-phonon coupling at reduced dimensionality. As a comparison, $\sigma(T)$ of $(PEA)_2(MA)Pb_2I_7$ initially increases with temperature at cryogenic region (80–120 K) and then decreases monotonically to a plateau of $\sigma_0^* \sim 1.46 \pm 0.01$ at 300 K, which is much smaller than that of $(PEA)_2(MA)Sn_2I_7$. $\sigma(T)$ of $(PEA)_2(MA)Pb_2I_7$ at low temperature (<120 K) where lattice is frozen and polaronic effect is negligible[50] can be well

https://doi.org/10.1038/s41467-024-52952-9

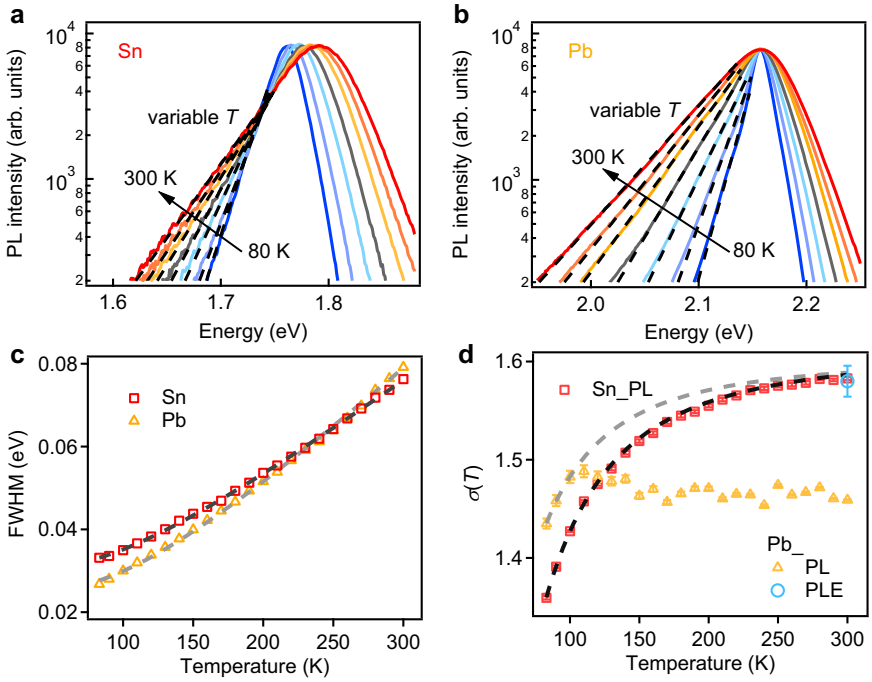

Fig. 5 | Analysis of temperature dependent PL spectra. PL spectra of (**a**) $(PEA)_2(MA)Sn_2I_7$ and (**b**) $(PEA)_2(MA)Pb_2I_7$ in a semi-log scale at different temperatures between 80 and 300 K. The black dashed lines represent the fit of Urbach tail by Eq. (4). **c** PL full-width-at-half-maximum (FWHM) as a function of temperature for $(PEA)_2(MA)Sn_2I_7$ (square) and its Pb counterpart (triangle) and the fit (dashed line) by Eq. (2). **d** Steepness factor $\sigma(T)$ as a function of temperature and the fit (dashed line) of the low temperature region by Eq. (5). The error bars represent fitting errors.

fitted by Eq. (5) (dashed line in Fig. 5d) and the deviation at high temperature indicates the excited state electronic and structural relaxation due to exciton-lattice coupling. As shown in Fig. 5d, the measured $\sigma(T)$ of $(PEA)_2(MA)Sn_2I_7$ exhibits slight deviation from the fitted curve at high temperature, indicating the presence but rather weak excited state polaronic effect in $(PEA)_2(MA)Sn_2I_7$. In contrast, the measured $\sigma(T)$ deviates significantly from the fitted curve at high temperatures for $(PEA)_2(MA)Pb_2I_7$, revealing prominent T-dependent excited state polaronic effect. To further confirm the fitted curve from low temperature σ_0^* in $(PEA)_2(MA)Pb_2I_7$, we also determined $\sigma_0{}^0$ from absorption tail by PL excitation (PLE) measurement at 300 K (see details in Supplementary Note 5) and the obtained $\sigma_0{}^0 \sim 1.58 \pm 0.02$ (blue circle) falls on the fitted curve.

Discussion

The determined photophysical parameters for $(PEA)_2(MA)Sn_2I_7$ and its Pb counterpart are summarized in Table 1. We also extracted the high-frequency dielectric constant ε_∞ along c axis and exciton effective mass from first-principles calculation for discussions (see Supplementary Note 6). $(PEA)_2(MA)Sn_2I_7$ and its Pb counterpart have same crystal structure with only different B site cations, which results in near identical ε_∞ and justifies similar $E_b{}^0$ of ~0.21 eV for $(PEA)_2(MA)Sn_2I_7$ and 0.22 eV for $(PEA)_2(MA)Pb_2I_7$ by steady-state optical measurement[56]. However, in-depth PL analysis reveals very different long- and short-range exciton-lattice coupling strength, as evidenced by γ_{LO} and σ_0^*. γ_{LO}, which is proportional to the long-range polarization response[20,31,51], is much smaller in $(PEA)_2(MA)Sn_2I_7$ than the Pb counterpart. Smaller γ_{LO} suggests less excited state structural relaxation in $(PEA)_2(MA)Sn_2I_7$, i.e., less displacement of excited-state potential energy surface (PES) relative to ground-state PES[21,57]. Meanwhile, σ_0^*, inversely proportional to short-range deformation potential, is much larger in $(PEA)_2(MA)Sn_2I_7$ (1.58 ± 0.01) than its Pb counterpart (1.46 ± 0.01), which also suggests much less excited state structural deformation in the former.

Table 1 | Comparison of the physical parameters of $(PEA)_2(MA)Sn_2I_7$ and its Pb counterpart

	$E_b{}^0$(eV)	$E_b{}^*$(eV)	γ_{LO}(eV)	$\sigma_0{}^*$	$m_u{}^*(m_0)$	ε_∞
$(PEA)_2(MA)Sn_2I_7$	0.21 ± 0.02	0.18 ± 0.02	0.072 ± 0.004	1.58 ± 0.01	0.07	4.7
$(PEA)_2(MA)Pb_2I_7$	0.22 ± 0.02	0.10 ± 0.01	0.095 ± 0.008	1.46 ± 0.01	0.13	4.5

A more intuitive way to understand σ_0^* is to compare it with the critical value σ_c of 1.42 for 2D materials, which determines the relative energy position and thus stability between band edge delocalized exciton and deformed Urbach exciton (UE)[17,52,58]. As σ_c is much smaller than σ_0^* of $(PEA)_2(MA)Sn_2I_7$ but similar to that of the Pb counterpart, UE state lies much higher than the band edge state in $(PEA)_2(MA)Sn_2I_7$ but close to that in $(PEA)_2(MA)Pb_2I_7$ (Fig. 6a, b)[17,52]. Therefore, compared to Pb counterpart with dynamic interconversion between band edge state and UE state, $(PEA)_2(MA)Sn_2I_7$ retains its band edge exciton with much weaker excited state polaronic effect (Fig. 6a). In the context of exciton polaron, electrons and holes with oppososing lattice deformation are mutually separated in real space. Specifically, the hole induces a compression of bonds, while the electron causes an elongation of bonds in metal halides[17,18,21]. Hence, weaker excited state polaronic effect in $(PEA)_2(MA)Sn_2I_7$ results in less polaronic screening effect and larger binding energy $E_b{}^*$, and vice versa for $(PEA)_2(MA)Pb_2I_7$. With $E_b{}^*$ of 0.18 eV for $(PEA)_2(MA)Sn_2I_7$, Saha-Langmuir equation (Supplementary Note 1) yields little exciton dissociation (7% at $n_0 = 10^{11}\,cm^{-2}$) at room temperature, which well explains the exciton recombination behavior. On the other hand, a $E_b{}^*$ of 0.10 eV for $(PEA)_2(MA)Pb_2I_7$ implies 35% exciton dissociation at $n_0 = 10^{11}\,cm^{-2}$ and a power factor β of 1.35 (Supplementary Note 1), which also agrees well with experimental value (1.31) from $TRPL_0$ results. This result aligns with earlier observations of elevated free-carrier densities in 2D lead halide perovskites. The measured densities surpass the values predicted by the Saha-Langmuir equation when using the exciton binding energy from the ground state[34,59,60]. This discrepancy highlights the

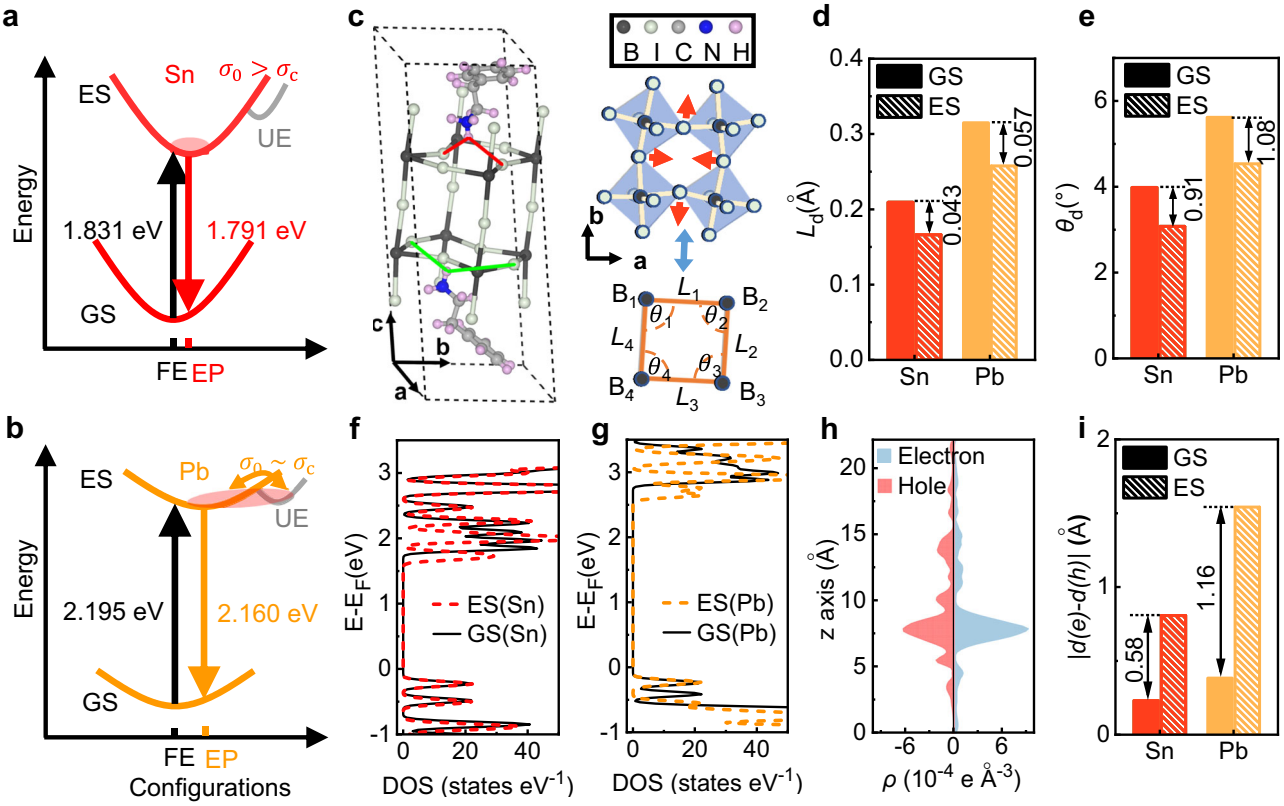

Fig. 6 | Calculation of exciton polaron in 2D metal halide perovskites. Scheme of potential energy surface labeled with ground state (GS), excited state (ES) and Urbach exciton (UE) states of (**a**) $(PEA)_2(MA)Sn_2I_7$ and (**b**) its Pb counterpart. **c** Illustrations of inter-octahedron distortion and the corresponding distortion descriptors including length displacement (L_d) and angle deviation (θ_d) in octahedral layers along *a*-*b* direction. The arrows denote the movement direction of the iodine atoms. The calculated (**d**) L_d and (**e**) θ_d of $(PEA)_2(MA)Sn_2I_7$ and $(PEA)_2(MA)Pb_2I_7$ (labeled as Sn and Pb) in GS and ES configurations. DOS of ground-state and excited-state configurations in (**f**) $(PEA)_2(MA)Sn_2I_7$ and (**g**) its Pb counterpart. **h** Summed electron (hole) densities in *a*-*b* plane ($\rho_i(z)$) as a function of *z* coordinate. **i** Effective distance between electron and hole along *z* coordinate in ground-state and excited-state configurations of $(PEA)_2(MA)Sn_2I_7$ and its Pb counterpart.

significant polaronic effect in the excited states of these materials. Meanwhile, Moser et al. have demonstrated exciton-exciton Auger heating contributes to the formation of long-lived free carriers[59], which might be the primary reason for the observation of non-negligible free carrier THz signals even at 4 K[34].

To substantiate the excited state polaronic effect and the screening of electron-hole interactions at atomic level, we conducted theoretical atomistic simulations employing density functional theory (DFT) and time-dependent density functional theory (TDDFT). These approaches allowed for the directly visualization of photo-induced structural and electronic relaxation at excited state[61]. The details of computational methods are provided in Supplementary Note 6. Briefly speaking, the primitive cell of $(PEA)_2(MA)Sn_2I_7$ or its Pb counterpart with experimental lattice parameters (Supplementary Table 2) was used to generate a $2\times2\times1$ supercell. With Perdew-Burke-Ernzerhof functional, the ground-state configurations were optimized by the DFT approach, followed by relaxation of the lowest-energy excited-state geometries through TDDFT approach. Given that the dielectric screening is weak along *c* axis, the density of states (DOS) and photogenerated electron-hole distributions were calculated by DFT and TDDFT, respectively, with optimally tuned and range-separated hybrid functional[62].

From the calculation, the iodine atoms in PbI_2 layers displace at excited state, with the concave and protruding iodine atoms moving towards straightening the Pb-I-Pb bonds (Fig. 6c). As a result, the distances between the concave (protruding) iodine atoms and the end $-NH_3$ of organic ligands, which are highlighted by red (green) lines in Fig. 6c, are increased (decreased). As distances guided by the red lines are 0.1–0.2 Å smaller than those guided by the green lines, the hydrogen bonds are overall weakened under photoexcitation. This agrees with the partial DOS where the valence and conduction band are predominantly contributed by the 5p orbital of iodine and the 5p (6p) orbital of Sn (Pb) cation (see details in Supplementary Note 6), respectively. Thereby, a fraction of electron densities transfers from iodine atoms to B site atoms under photoexcitation, attenuating hydrogen bonding.

We quantify the overall light-induced structural changes in $(PEA)_2(MA)Sn_2I_7$ and its Pb counterpart by a set of inter-octahedron geometry descriptors including length displacement L_d and angle deviation θ_d[63]

$$L_d = \sum_{i=1}^{N} |L_i - L| \tag{6}$$

$$\theta_d = \sum_{i=1}^{N} |90 - \theta_i| \tag{7}$$

where L_i is the distance between two adjacent B site atom (B-B), θ_i is the right angle of B-B-B and L denotes the average value of all L_i at a-b plane (Fig. 6c). The L_d and θ_d for $(PEA)_2(MA)Sn_2I_7$ and the Pb counterpart at both ground-state and relaxed excited-state configurations are calculated and plotted in Fig. 6d, e, respectively. Interestingly, both materials exhibit reductions of L_d and θ_d at excited-state relative to ground state, which is consistent with very recent experimental results showing photoexcitation-induced lattice straightening in lead

halide perovskites[64]. Importantly, $(PEA)_2(MA)Sn_2I_7$ shows less change of L_d and θ_d at excited state compared to the Pb counterpart. On the other hand, the electronic structure change can be captured by the change of DOS in Fig. 6f, g. The conduction band edge at excited-state shifts down compared to ground-state in both materials and the shift is less in $(PEA)_2(MA)Sn_2I_7$ than the Pb counterpart. These calculations on ground state and excited state nuclear and electronic structures confirm less excited state relaxation in $(PEA)_2(MA)Sn_2I_7$.

The excited state polaronic effect on the screening of electron-hole interaction can be scrutinized by calculating the distance between electron and hole, $|d(e) - d(h)|$. The effective positions of electron and hole along c direction can be defined as

$$d = \frac{\sum_i z\rho_i(z)}{\sum_i \rho_i(z)} \quad (8)$$

where z denotes the coordinate along c direction and the $\rho_i(z)$ represents the summed electron (hole) densities in a-b plane at z coordinate (Fig. 6h). As shown in Fig. 6i where we compare electron-hole separation at ground and excited state configurations, the distance between electron and hole are increased at excited state in both 2D tin- and lead-halide perovskites and the separation is significantly smaller in $(PEA)_2(MA)Sn_2I_7$. This electron-hole separation at excited state, together with geometric and electronic structure above, directly confirms excited state polaronic effect screens electron-hole interaction in both materials, forming exciton polaron and the polaronic screening effect is much weaker in $(PEA)_2(MA)Sn_2I_7$ than in the Pb counterpart.

To unveil the ultimate structural origin for different excited state polaronic effect in $(PEA)_2(MA)Sn_2I_7$ and the Pb counterpart, we calculated the orientation-dependent Young's modulus in a-b plane, which reflects the material stiffness (see Supplementary Note 6 for details)[65]. Notably, Young's modulus along a and b axis in $(PEA)_2(MA)Sn_2I_7$ is ~90% and ~65% larger than that in Pb counterpart. The much larger Young's modulus in $(PEA)_2(MA)Sn_2I_7$ indicates a more stiffened and less deformable lattice, which can be attributed to the shorter Sn-I bond. Furthermore, the exciton effective mass of $(PEA)_2(MA)Sn_2I_7$ is about half of that in the Pb counterpart. A larger effective mass implies a narrower electronic structural bandwidth and stronger exciton-phonon coupling strength, which tends to drive polaron formation[17,21,57].

To preclude external factors, we have performed additional $TRPL_0$ (Supplementary Fig. 9) and temperature dependent spin relaxation (Supplementary Fig. 10) measurements and analysis on different sets of $(PEA)_2(MA)Sn_2I_7$ flakes and its Pb counterparts and observed similar excited state recombination and spin relaxation behaviors as observed above. We have also compared 2D tin- and lead-halide perovskites with different n ($n = 1$ and 3, Supplementary Figs. 11, 12, 13) and different long-chain ligands (BA^+: butylammonium, $2T^+$: bithiophenylethylammonium and $3T^+$: 2-([2,2′:5′,2″-terthiophen]-5-yl)ethan-1-aminium, $n = 2$) (Supplementary Fig. 14). For $n = 2$ and $n = 3$ perovskites, we have observed consistently excitonic behavior in tin halide perovskites but partial free carrier behavior due to much weakened electron-hole interaction in Pb counterparts, indicating a fairly robust exciton in 2D tin halide perovskites rather than their Pb counterparts. Interestingly, we note both $n = 1$ tin- and lead- halide perovskites exhibit a linear $TRPL_0$ dependence on photoexcitation density at room temperature, indicating persistently bound electron-hole pair and strong excitonic effect in both $n = 1$ perovskites at room temperature. This is reasonable since the $n = 1$ inorganic layer is too thin to screen electron-hole binding energy sufficiently to be comparable to k_BT at room temperature. As a contrast, previous studies on 2D and 3D tin halide perovskites have suggested a lower E_b than their Pb counterparts[7,24–28]. In 3D tin halide perovskites, the more stiffened Sn-I lattice and lighter Sn element should lead to higher optical phonon frequencies υ_{Sn-I} which can reach the exciton characteristic frequency $\upsilon_b = E_b/\hbar$ and thus excitons in 3D tin halide perovskites experience more effective screening by the ionic metal-halide lattice[26–28]. Although υ_b increases dramatically and gets out of optical phonon frequencies from 3D to 2D, the smaller exciton effective mass and band gap still imply a smaller exciton binding energy in 2D tin halide perovskites than the Pb counterparts[7,24,25]. These results highlight excited state polaronic screening effect, rather than ground state properties, govern the photogenerated exciton nature and dynamics. In contrast to Pb counterpart with free carrier characteristics, the robust exciton with weak exciton-phonon coupling defines 2D tin halide perovskites as genuine excitonic semiconductors, which greatly benefits their optoelectronic applications, especially for light emission purposes. The robust excitonic effect facilitates the encounter and radiative recombination of photo- or electric- injected electron and hole carriers and inhibits the reverse exciton thermal dissociation. This, together with higher carrier mobility[11,12] and color purity due to weak exciton-phonon coupling, is ideal for light emission and lasing applications.

In conclusion, we have performed a combined spectroscopy and theoretical study on the excited state exciton nature and dynamics in high-quality 2D tin halide perovskites by comparing to the Pb counterpart. Despite both exhibiting a same large E_b^0 ~ 0.2 eV from steady state exciton Rydberg series measurement, we reveal a much weaker long- and short-range exciton-phonon coupling in 2D tin halide perovskites than the Pb counterpart, resulting in weak excited state polaronic screening effect and the persistence of robust excitons in 2D tin halide perovskites. The excited state exciton binding energy in $n = 2$ 2D tin halide perovskites has been determined to be ~0.18 eV, about twice of that in the Pb counterpart with same structure. This finding challenges the conventional view of exciton behavior and highlights the critical role of excited state polaronic effect on exciton nature and dynamics in these materials. The robust excitons at excited state in 2D tin halide perovskites exhibits excitation power-insensitive, high-efficiency and high color-purity light emission, rendering them superior for light-emitting diodes and lasers than their Pb counterparts.

Methods

Preparation of perovskite single crystals

All single crystals were grown using the slow cooling method[5]. For $(PEA)_2(MA)Sn_2I_7$, 0.17 mmol phenethylammonium iodide (PEAI, Greatcell Solar Ltd.), 0.4 mmol methylammonium iodide (MAI, Greatcell Solar Ltd.) and 0.4 mmol SnI_2 (Shanghai Macklin Biochemical Co., Ltd.) were added into 1 mL hydriodic acid (HI, 57wt.%, TCI) and 0.1 mL hypophosphorous acid (H_3PO_2, J&K Scientific). For $(PEA)_2(MA)_2Sn_3I_{10}$, 0.17 mmol PEAI, 0.67 mmol MAI and 0.4 mmol SnI_2 were added into 1 mL HI and 0.1 mL H_3PO_2. For $(PEA)_2(MA)Pb_2I_7$, 0.43 mmol PEAI, 0.60 mmol MAI and 0.59 mmol PbI_2 (TCI (Shanghai) Development Co., Ltd.) were added into 0.9 mL HI and 0.1 mL H_3PO_2. For $(PEA)_2(MA)_2Pb_3I_{10}$, 0.15 mmol PEAI, 0.53 mmol MAI and 0.59 mmol PbI_2 were added into 0.8 mL HI and 0.1 mL H_3PO_2. As for $(BA)_2(MA)Sn_2I_7$, $(2T)_2(MA)Sn_2I_7$ and $(3T)_2(MA)Sn_2I_7$ single crystals, they were synthesized using the previously reported recipes[5]. After heating and complete dissolution, they were put into a muffle furnace for cooling down from 383 K to 293 K at a cooling rate of 1 °C/h, and finally high purity halide perovskite single crystals were obtained. It is worth noting that all the processes, starting from the weighing of precursors and ending with the drying of single crystals, are conducted within N_2 glove box. The CCDC numbers for $(PEA)_2(MA)Sn_2I_7$ and $(PEA)_2(MA)Pb_2I_7$ are 2240837 and 2299252, respectively. 2D perovskites and h-BN (Onway Technology) thin flakes were mechanically exfoliated onto gel films (Gel-Pak PF-X4) from bulk single crystals. Under an optical microscope, we fabricated BN/perovskites/BN heterostructures to preserve 2D perovskites from the damage caused by water, oxygen and vacuum by transferring the exfoliated thin flakes from gel film to SiO_2 substrate in sequence[29]. The whole processes are operated in N_2 glovebox.

Steady state optical measurements

We used a home-built microscope setup integrated with liquid-nitrogen-cooled cryostat (custom-made STC-W30, LANHAI Science Instrument) for optical characterizations and the samples are consistently in controlled environment of vacuum or N_2. The TeslatronPT VTI cryostat (Oxford Instruments Inc., temperature range from 4 to 300 K) was utilized for reflection spectra at Ultra-low temperature (4 K) with a home-made optical probe inserts with a 50X objective lens (MPlan 50X, Olympus, NA = 0.75) seated on the probe for the optical excitation and collection. A broadband halogen lamp (OSLR, Thorlabs, Inc.) is used as the light source. In steady-state absorption measurement, the fundamental 1030 nm femtosecond-pulsed laser (CARBIDE, Light Conversion Ltd) was focused onto a YAG (Yttrium Aluminum Garnet) crystal for generating a continuum white light. The steady-state transmission and reflection differential spectra were obtained by normalizing the transmitted ($\delta T = (T_{\mathrm{sample}} - T_{\mathrm{sub}})/T_{\mathrm{sub}}$) and reflected ($\delta R = (R_{\mathrm{sample}} - R_{\mathrm{sub}})/R_{\mathrm{sub}}$) light from the sample on transparent SiO_2 substrate to that from the bare substrate, respectively. And The collection and analysis of transmitted and reflected light were conducted by liquid nitrogen cooled detectors (PyLon 100B, Princeton Instruments). The absorption coefficient of sample was calculated by $A = 1 - (T_{\mathrm{sample}} + R_{\mathrm{sample}})/(T_{\mathrm{sub}} + R_{\mathrm{sub}})$. In PL measurement, PL spectra were obtained with a 532 nm continuous-wave (CW) laser excitation. A supercontinuum laser (SC-OEM, YSL Photonics) coupled with a monochromator was used as excitation light source for PL excitation measurements.

Time-resolved photoluminescence measurements

The fundamental 1030 nm femtosecond-pulsed laser (pulse width ~200 fs and frequency of 100–1000 KHz, YactoFiber-FL-20, YactoTech) was focused onto a barium metaborate (BBO) crystal to generate a 515 nm excitation light for TRPL measurements. The TRPL decay kinetics were collected using a TCSPC module (SPC-130INX) and ultrafast detector (Hybrid PMT, HPM-100-07) with an instrument response function ~30 ps.

Spin-resolved transient absorption spectroscopy

For TA measurements, two 1030 nm femtosecond-pulsed lasers (~150 fs pulse duration, supplied by CARBIDE, Light Conversion Ltd) were focused onto YAG (Yttrium Aluminum Garnet) crystals, producing a continuum white light. One served as the probe light, and the other was filtered to selected central wavelength with narrow FWHM (i.e., 640–660 nm) and served as the pump light. To accurately regulate the time delay between the pump and probe beams, a high-precision motorized delay stage from Newport was employed. Both beams were converged and focused by a microscope equipped with a 50X transmissive lens, resulting in spot size smaller than 2 μm. The transmitted probe light, with the pump beam efficiently filtered out, was detected by liquid nitrogen cooled detectors (PyLon 100B, Princeton Instrument). The TA signal ($\Delta T/T$) was derived by normalizing the spectral intensity from the pumped to the unpumped state, yielding $\delta T = \Delta T/T = (T_{\mathrm{pump\ on}} - T_{\mathrm{pump\ off}})/T_{\mathrm{pump\ off}}$. For the spin-resolved transient absorption measurement, circularly polarized lights were generated by passing the linear polarized pump and probe beams through a quarter wave plate (1/4λ). By manipulating the pump beam's polarization direction using a half wave plate, either same (SCP) or opposite (OCP) circular polarization conditions could be achieved relative to the probe beam. Throughout all optical measurements, the laser beam was focused to a spot size of less than 2 μm.

Data availability

All data to evaluate the conclusions are present in the manuscript and the Supplementary Material. Raw data are available from the corresponding authors on request.

References

1. Han, D. et al. Tautomeric mixture coordination enables efficient lead-free perovskite LEDs. *Nature* **622**, 493–498 (2023).
2. Morteza Najarian, A. et al. Homomeric chains of intermolecular bonds scaffold octahedral germanium perovskites. *Nature* **620**, 328–335 (2023).
3. Park, J. Y. et al. Thickness control of organic semiconductor-incorporated perovskites. *Nat. Chem.* **15**, 1745–1753 (2023).
4. Lei, Y. et al. Perovskite superlattices with efficient carrier dynamics. *Nature* **608**, 317–323 (2022).
5. Li, Y. et al. Phase-pure 2D tin halide perovskite thin flakes for stable lasing. *Sci. Adv.* **9**, eadh0517 (2023).
6. Gu, H. et al. Phase-pure two-dimensional layered perovskite thin films. *Nat. Rev. Mater.* **8**, 533–551 (2023).
7. Hansen, K. R. et al. Mechanistic origins of excitonic properties in 2D perovskites: Implications for exciton engineering. *Matter* **6**, 3463–3482 (2023).
8. Passarelli, J. V. et al. Tunable exciton binding energy in 2D hybrid layered perovskites through donor-acceptor interactions within the organic layer. *Nat. Chem.* **12**, 672–682 (2020).
9. Metcalf, I. et al. Synergy of 3D and 2D perovskites for durable, efficient solar cells and beyond. *Chem. Rev.* **123**, 9565–9652 (2023).
10. Mihalyi-Koch, W. et al. Tuning structure and excitonic properties of 2D Ruddlesden–Popper germanium, tin, and lead iodide perovskites via interplay between cations. *J. Am. Chem. Soc.* **145**, 28111–28123 (2023).
11. Liu, A. et al. High-performance metal halide perovskite transistors. *Nat. Electron.* **6**, 559–571 (2023).
12. Liang, A. et al. Ligand-driven grain engineering of high mobility two-dimensional perovskite thin-film transistors. *J. Am. Chem. Soc.* **143**, 15215–15223 (2021).
13. Quan, L. N. et al. Vibrational relaxation dynamics in layered perovskite quantum wells. *Proc. Natl Acad. Sci. USA* **118**, e2104425118 (2021).
14. Zhang, H. et al. Ultrafast relaxation of lattice distortion in two-dimensional perovskites. *Nat. Phys.* **19**, 545–550 (2023).
15. Thouin, F. et al. Phonon coherences reveal the polaronic character of excitons in two-dimensional lead halide perovskites. *Nat. Mater.* **18**, 349–356 (2019).
16. Sun, Q. et al. Ultrafast and high-yield polaronic exciton dissociation in two-dimensional perovskites. *J. Am. Chem. Soc.* **143**, 19128–19136 (2021).
17. Srimath Kandada, A. R. & Silva, C. Exciton polarons in two-dimensional hybrid metal-halide perovskites. *J. Phys. Chem. Lett.* **11**, 3173–3184 (2020).
18. Tao, W., Zhang, Y. & Zhu, H. Dynamic exciton polaron in two-dimensional lead halide perovskites and implications for optoelectronic applications. *Acc. Chem. Res.* **55**, 345–353 (2022).
19. Simbula, A. et al. Exciton dissociation in 2D layered metal-halide perovskites. *Nat. Commun.* **14**, 4125 (2023).
20. Buizza, L. R. V. & Herz, L. M. Polarons and charge localization in metal-halide semiconductors for photovoltaic and light-emitting devices. *Adv. Mater.* **33**, e2007057 (2021).
21. Fu, J., Ramesh, S., Melvin Lim, J. W. & Sum, T. C. Carriers, quasiparticles, and collective excitations in halide perovskites. *Chem. Rev.* **123**, 8154–8231 (2023).
22. Neutzner, S. et al. Exciton-polaron spectral structures in two-dimensional hybrid lead-halide perovskites. *Phys. Rev. Mater.* **2**, 064605 (2018).
23. Kahmann, S. et al. Photophysics of two-dimensional perovskites—learning from metal halide substitution. *Adv. Funct. Mater.* **31**, 2103778 (2021).

24. Hansen, K. R. et al. Low exciton binding energies and localized exciton–polaron states in 2D tin halide perovskites. *Adv. Opt. Mater.* **10**, 2102698 (2022).
25. Dyksik, M. et al. Broad tunability of carrier effective masses in two-dimensional halide perovskites. *ACS Energy Lett.* **5**, 3609–3616 (2020).
26. Milot, R. L. et al. The effects of doping density and temperature on the optoelectronic properties of formamidinium tin triiodide thin films. *Adv. Mater.* **30**, 1804506 (2018).
27. Umari, P., Mosconi, E. & De Angelis, F. Infrared dielectric screening determines the low exciton binding energy of metal-halide perovskites. *J. Phys. Chem. Lett.* **9**, 620–627 (2018).
28. Herz, L. M. How lattice dynamics moderate the electronic properties of metal-halide perovskites. *J. Phys. Chem. Lett.* **9**, 6853–6863 (2018).
29. Zhou, H. et al. Spatiotemporally coupled electron-hole dynamics in two dimensional heterostructures. *Nano Lett.* **22**, 2547–2553 (2022).
30. Zhang, T. et al. Regulation of the luminescence mechanism of two-dimensional tin halide perovskites. *Nat. Commun.* **13**, 60 (2022).
31. Wright, A. D. et al. Electron–phonon coupling in hybrid lead halide perovskites. *Nat. Commun.* **7**, 11755 (2016).
32. Chernikov, A. et al. Exciton binding energy and nonhydrogenic Rydberg series in monolayer WS2. *Phys. Rev. Lett.* **113**, 076802 (2014).
33. Blancon, J. C. et al. Scaling law for excitons in 2D perovskite quantum wells. *Nat. Commun.* **9**, 2254 (2018).
34. Motti, S. G. et al. Exciton formation dynamics and band-like free charge-carrier transport in 2D metal halide perovskite semiconductors. *Adv. Funct. Mater.* **33**, 2300363 (2023).
35. Tao, W., Zhou, Q. & Zhu, H. Dynamic polaronic screening for anomalous exciton spin relaxation in two-dimensional lead halide perovskites. *Sci. Adv.* **6**, eabb7132 (2020).
36. Xing, G. et al. Transcending the slow bimolecular recombination in lead-halide perovskites for electroluminescence. *Nat. Commun.* **8**, 14558 (2017).
37. Konabe, S. Screening effects due to carrier doping on valley relaxation in transition metal dichalcogenide monolayers. *Appl. Phys. Lett.* **109**, 073104 (2016).
38. Maialle, M. Z., de Andrada e Silva, E. A. & Sham, L. J. Exciton spin dynamics in quantum wells. *Phys. Rev. B* **47**, 15776–15788 (1993).
39. Miyauchi, Y. et al. Evidence for line width and carrier screening effects on excitonic valley relaxation in 2D semiconductors. *Nat. Commun.* **9**, 2598 (2018).
40. Mahmood, F., Alpichshev, Z., Lee, Y. H., Kong, J. & Gedik, N. Observation of exciton-exciton interaction mediated valley depolarization in monolayer MoSe2. *Nano Lett.* **18**, 223–228 (2018).
41. Zhu, C. R. et al. Exciton valley dynamics probed by Kerr rotation in WSe2 monolayers. *Phys. Rev. B* **90**, 161302(R) (2014).
42. Giovanni, D. et al. Coherent spin and quasiparticle dynamics in solution-processed layered 2D lead halide perovskites. *Adv. Sci.* **5**, 1800664 (2018).
43. Zhou, H., Chen, Y. & Zhu, H. Deciphering asymmetric charge transfer at transition metal dichalcogenide-graphene interface by helicity-resolved ultrafast spectroscopy. *Sci. Adv.* **7**, eabg2999 (2021).
44. Chen, X. et al. Tuning spin-polarized lifetime in two-dimensional metal-halide perovskite through exciton binding energy. *J. Am. Chem. Soc.* **143**, 19438–19445 (2021).
45. Giovanni, D. et al. Highly spin-polarized carrier dynamics and ultralarge photoinduced magnetization in CH3NH3PbI3 perovskite thin films. *Nano Lett.* **15**, 1553–1558 (2015).
46. Bourelle, S. A. et al. How exciton interactions control spin-depolarization in layered hybrid perovskites. *Nano Lett.* **20**, 5678–5685 (2020).
47. Liang, W. et al. Efficient optical orientation and slow spin relaxation in lead-free CsSnBr3 perovskite nanocrystals. *ACS Energy Lett.* **6**, 1670–1676 (2021).
48. Huang, Y. et al. Tuning spin-polarized lifetime at high carrier density through deformation potential in Dion-Jacobson-phase perovskites. *J. Am. Chem. Soc.* **146**, 12225–12232 (2024).
49. Lagarde, D. et al. Carrier and polarization dynamics in monolayer MoS2. *Phys. Rev. Lett.* **112**, 047401 (2014).
50. Guo, Y. et al. Dynamic emission Stokes shift and liquid-like dielectric solvation of band edge carriers in lead-halide perovskites. *Nat. Commun.* **10**, 1175 (2019).
51. Rudin, S., Reinecke, T. & Segall, B. Temperature-dependent exciton linewidths in semiconductors. *Phys. Rev. B* **42**, 11218–11231 (1991).
52. Tao, W., Zhang, C., Zhou, Q., Zhao, Y. & Zhu, H. Momentarily trapped exciton polaron in two-dimensional lead halide perovskites. *Nat. Commun.* **12**, 1400 (2021).
53. Huang, X. et al. Understanding electron-phonon interactions in 3D lead halide perovskites from the stereochemical expression of 6s(2) lone pairs. *J. Am. Chem. Soc.* **144**, 12247–12260 (2022).
54. Handa, T., Aharen, T., Wakamiya, A. & Kanemitsu, Y. Radiative recombination and electron-phonon coupling in lead-free CH3NH3SnI3 perovskite thin films. *Phys. Rev. Mater.* **2**, 075402 (2018).
55. Ledinsky, M. et al. Temperature dependence of the Urbach energy in lead iodide perovskites. *J. Phys. Chem. Lett.* **10**, 1368–1373 (2019).
56. Filip, M. R., Qiu, D. Y., Del Ben, M. & Neaton, J. B. Screening of excitons by organic cations in quasi-two-dimensional organic-inorganic lead-halide perovskites. *Nano Lett.* **22**, 4870–4878 (2022).
57. Iaru, C. M. et al. Frohlich interaction dominated by a single phonon mode in CsPbBr(3). *Nat. Commun.* **12**, 5844 (2021).
58. Schreiber, M. & Toyozawa, Y. Numerical experiments on the absorption lineshape of the exciton under lattice vibrations. III. The Urbach rule. *J. Phys. Soc. Jpn.* **51**, 1544–1550 (1982).
59. Burgos-Caminal, A., Socie, E., Bouduban, M. E. F. & Moser, J.-E. Exciton and carrier dynamics in two-dimensional perovskites. *J. Phys. Chem. Lett.* **11**, 7692–7701 (2020).
60. Balogun, F. H. et al. Untangling free carrier and exciton dynamics in layered hybrid perovskites using ultrafast optical and terahertz spectroscopy. *Mater. Res. Express* **11**, 025503 (2024).
61. Zhang, X., Lu, G., Baer, R., Rabani, E. & Neuhauser, D. Linear-response time-dependent density functional theory with stochastic range-separated hybrids. *J. Chem. Theory Comput.* **16**, 1064–1072 (2020).
62. Refaely-Abramson, S., Jain, M., Sharifzadeh, S., Neaton, J. B. & Kronik, L. Solid-state optical absorption from optimally tuned time-dependent range-separated hybrid density functional theory. *Phys. Rev. B* **92**, 081204(R) (2015).
63. Han, X. B., Jing, C. Q., Zu, H. Y. & Zhang, W. Structural descriptors to correlate Pb ion displacement and broadband emission in 2D halide perovskites. *J. Am. Chem. Soc.* **144**, 18595–18606 (2022).
64. Yazdani, N. et al. Coupling to octahedral tilts in halide perovskite nanocrystals induces phonon-mediated attractive interactions between excitons. *Nat. Phys.* **20**, 47–53 (2024).
65. Wang, V. & Geng, W. T. Lattice defects and the mechanical anisotropy of borophene. *J. Phys. Chem. C.* **121**, 10224–10232 (2017).

Acknowledgements

We thank Zhihao Gong and Hua Wang at ZJU-Hangzhou Global Scientific and Technological Innovation Center for help with theoretical studies. H. Zhu thanks the financial support from the National Natural Science Foundation of China (22273084, H.Z.) and Department of Science and Technology of Zhejiang Province (2024C01191, H.Z.). G.Nan acknowledges the National Natural Science Foundation of China (22273088, G.N.), Hefei National Research Center for Physical Sciences at the Microscale (KF2021004, G.N.) and Scientific Research Fund of Zhejiang Provincial Education Department (Y202250336, G.N.). H. Zhou thanks

the financial support from the China Postdoctoral Science Foundation (Grant No.2022M722727, H.Z.). This study is supported by the open fund of the state key laboratory of molecular reaction dynamics in DICP, CAS.

Author contributions

H.Zhou and H.Zhu. conceived the project. H.Zhou conducted steady-state PL, TRPL and TA measurements. Q.Feng and G.Nan conducted the theoretical calculations. Y.L. and E.S. synthesized single-crystal samples. W.Tang and L.Li helped collect the reflectance spectra at 4 K. C.Sun helped collect the PLQY. W.Tao participated in data analysis. H.Zhou, H.Zhu, Q.Feng, G.Nan wrote the manuscript. All authors read and revised the manuscript.

Competing interests

The authors declare no competing interests.

Additional information

Supplementary information The online version contains supplementary material available at https://doi.org/10.1038/s41467-024-52952-9.

Correspondence and requests for materials should be addressed to Guangjun Nan or Haiming Zhu.

Peer review information *Nature Communications* thanks Kameron Hansen, Michele Saba and the other anonymous reviewer(s) for their contribution to the peer review of this work. A peer review file is available.

Reprints and permissions information is available at http://www.nature.com/reprints

Publisher's note Springer Nature remains neutral with regard to jurisdictional claims in published maps and institutional affiliations.

Open Access This article is licensed under a Creative Commons Attribution-NonCommercial-NoDerivatives 4.0 International License, which permits any non-commercial use, sharing, distribution and reproduction in any medium or format, as long as you give appropriate credit to the original author(s) and the source, provide a link to the Creative Commons licence, and indicate if you modified the licensed material. You do not have permission under this licence to share adapted material derived from this article or parts of it. The images or other third party material in this article are included in the article's Creative Commons licence, unless indicated otherwise in a credit line to the material. If material is not included in the article's Creative Commons licence and your intended use is not permitted by statutory regulation or exceeds the permitted use, you will need to obtain permission directly from the copyright holder. To view a copy of this licence, visit http://creativecommons.org/licenses/by-nc-nd/4.0/.

© The Author(s) 2024